ADVANCING EARTH AND SPACE SCIENCES

Geophysical Research Letters

RESEARCH LETTER
10.1029/2025GL116255

# MAVEN Observations of Metallic $Fe^+$ Distributions in the Martian Ionosphere

**A. R. Poppe[1], G. A. Collinson[2], M. Benna[2,3], S. W. Stone[2], J. M. C. Plane[4], C. M. Fowler[5], and S. Xu[1]**

[1]Space Sciences Laboratory, University of California, Berkeley, Berkeley, CA, USA, [2]NASA Goddard Space Flight Center, Greenbelt, MD, USA, [3]CSST, University of Maryland, Baltimore, MD, USA, [4]School of Chemistry, University of Leeds, Leeds, UK, [5]Department of Physics and Astronomy, West Virginia University, Morgantown, WV, USA

**Key Points:**

- MAVEN/NGIMS observes $Fe^+$ in the martian ionosphere at altitudes between 120 and 180 km across almost six (Earth) years
- $Fe^+$ density profiles during Deep Dip observations are highly variable likely due to changing underlying atmospheric/ionospheric conditions
- Global $Fe^+$ distributions are uniform to first order with moderate declines on the nightside and in the northern hemisphere near perihelion

**Supporting Information:**

Supporting Information may be found in the online version of this article.

**Correspondence to:**

A. R. Poppe,
poppe@berkeley.edu

**Citation:**

Poppe, A. R., Collinson, G. A., Benna, M., Stone, S. W., Plane, J. M. C., Fowler, C. M., & Xu, S. (2025). MAVEN observations of metallic $Fe^+$ distributions in the martian ionosphere. *Geophysical Research Letters*, *52*, e2025GL116255. https://doi.org/10.1029/2025GL116255

Received 31 MAR 2025
Accepted 16 JUN 2025

## Abstract

Metallic ions deposited in planetary atmospheres via meteoroid ablation are an invaluable tool for understanding electric fields, atmospheric winds, and minor ion transport. At Mars, metallic ion distributions are poorly understood. We analyze MAVEN/NGIMS $Fe^+$ distributions in the Martian ionosphere over the period of 2015–2020 at altitudes ~120–200 km. The $Fe^+$ vertical structure observed during individual low-altitude MAVEN Deep Dip campaigns is highly variable likely due to variations in the ion magnetization altitude and corresponding ion transport conditions. Deep Dip campaigns on or near the martian nightside show evidence for in situ production of $Fe^+$ ions via electron precipitation. On average, $Fe^+$ ions are globally distributed in the martian ionosphere at altitudes >120 km with only slight decreases on the martian nightside and in the southern hemisphere. We find a similar, albeit less intense, decrease in the $Fe^+$ densities in the northern hemisphere near perihelion as has been reported for $Mg^+$.

## Plain Language Summary

All objects in the solar system are continuously bombarded by interplanetary meteoroids. When meteoroids enter the atmosphere of a planet, they heat up and shed atoms at high altitudes through a process called "ablation." The resulting metallic ions, such as iron ($Fe^+$), have lifetimes of many days and serve as important tracers for understanding electric fields and winds in the upper atmosphere. In this study, we analyze measurements of $Fe^+$ ions from the entire MAVEN mission, up through 2020 when the spacecraft's periapsis was raised above the altitudes where metallic ions are observed. We find that metal ions have a range of vertical distributions at different locations and times at Mars that are likely explained by changes in the way ions are transported vertically in the atmosphere. We also find that $Fe^+$ ions are largely evenly distributed around the planet, with a slight decrease at night. Additionally, we observe weak seasonal variations in the presence of metallic ions. These findings expand our understanding of Mars' atmospheric composition and dynamics. This research has implications for our broader understanding of planetary atmospheres and the effects of exogenous material on their composition and behavior.

## 1. Introduction

All planetary atmospheres in the solar system are subject to a continuous flux of hyper-velocity interplanetary dust grains that deposit exogenous material via meteoroid ablation (e.g., Carrillo-Sánchez et al., 2016, 2020, 2022; Moses, 1992; Moses & Poppe, 2017; Plane, Flynn, et al., 2018). An important consequence of this effect is the injection of metallic species (e.g., $Na/Na^+$, $Mg/Mg^+$, $Fe/Fe^+$, etc.) into planetary atmospheres, thereby altering their composition and photochemistry (e.g., Aikin & Goldberg, 1973; Pesnell & Grebowsky, 2000; Plane, Flynn, et al., 2018; Whalley & Plane, 2010). Exogenic metallic species in planetary atmospheres also play a critical role in the formation of high altitude clouds via introduction of meteoric smoke particles that can serve as condensation nuclei for cloud particles (e.g., Gumbel & Megner, 2009; Hartwick et al., 2019; Listowski et al., 2014; Megner & Gumbel, 2009; Plane, Carrillo-Sánchez, et al., 2018). At Earth, such metal ion distributions have long been observed (e.g., Grebowsky & Aikin, 2002, and refs. therein) and observations of sporadic electron density layers at low altitudes in Mars' ionosphere have been interpreted as meteoric metallic ion layers (e.g., Haider et al., 2013; Pätzold et al., 2005; Withers et al., 2008, 2013), although remote-sensing indicates insufficient $Mg^+$ densities and localized ionization may instead explain these layers (Crismani et al., 2019). More recently, the presence of metal ions in the atmosphere of Mars has been explicitly confirmed via remote-sensing and in situ observations by the MAVEN spacecraft (Benna et al., 2015; Crismani et al., 2017, 2023; Grebowsky et al., 2017).

In an earlier study, Grebowsky et al. (2017) reported observations of apparently unique, non-Earthlike behavior in meteoric $Mg^+$ and $Fe^+$ ions in the ionosphere of Mars taken by the MAVEN Neutral Gas and Ion Mass Spectrometer (NGIMS; Mahaffy et al., 2015). Among other things, this behavior included a close correspondence between the metallic ion scale heights and the background neutral $CO_2$ scale heights. At altitudes above the homopause, which at Mars varies between ∼60−120 km (Slipski et al., 2018; Yoshida et al., 2020), turbulent diffusion that mixes all atmospheric species should taper off in favor of gravitational separation of species according to their masses. The apparent lack of such mass-dependent separation and the close correspondence between the metallic ion and neutral $CO_2$ scale heights led Grebowsky et al. (2017) to suggest that either new ionospheric or atmospheric sources of metallic ions should be considered or that our understanding of the upwards transport of metallic ions at Mars lacked critical, as-of-yet unknown mechanisms. Since this report, these puzzling observations do not appear to have been further studied.

Here, we analyze the full set of MAVEN/NGIMS observations of $Fe^+$ ions, focusing on the individual MAVEN Deep Dip (DD) observations as well as the overall distributions of $Fe^+$ ions with respect to several controlling variables. We analyze $Fe^+$ in particular as it is one of the most abundant metallic ion species present in the martian ionosphere and does not overlap in mass with other known photochemical species. Investigation of other species observed by NGIMS, in particular $Mg^+$ (masses 24, 25, 26 amu), is deferred for later work due to the presence of higher background counts that complicates the analysis and interpretation. In Section 2, we describe the data reduction and draw an important distinction between our data processing methodology and that used in Grebowsky et al. (2017). We present the distributions of $Fe^+$ ions in Section 3, focusing first on observations during the nine MAVEN DD campaigns before moving to overall average distributions as a function of altitude, local time, solar zenith angle, latitude, and orbital phase. We discuss these results and qualitatively compare to previous remote-sensing observations of metallic ion layers in Mars' ionosphere in Section 4 and conclude in Section 5.

## 2. MAVEN/NGIMS Metallic Ion Observations

### 2.1. Data Processing and Background Calculation

We start with the MAVEN/NGIMS Level 1B (L1B) data products available through the NASA Planetary Data System to compile the $Fe^+$ ion observations. NGIMS L1B observations are provided in count rates (counts $s^{-1}$) and are converted to ion densities via a constant calibration coefficient, $C = 0.0673$ $cm^{-3}$ per count $s^{-1}$. We included observations from January 2015, when routine NGIMS metallic ion observations commenced, through September 2020, when the MAVEN periapsis raise and associated NGIMS operational changes severely limited any continuing metallic ion observations. From all available metallic ion observations, we discarded any observations that were taken (a) during off-nominal NGIMS boresight pointing of >2°, such as during neutral wind scans (Benna et al., 2019), (b) during periods when the spacecraft potential exceeded ±3 V, which alters the ion inflow into the instrument, or (c) during periods where neutral densities were sufficiently high (>∼$10^{11}$ $cm^{-3}$) to induce scattering within the instrument. A background count level was identified in the NGIMS ion measurements via concurrent count-rate measurements taken at mass 75 amu, where no major species are known to exist. This background count level, which varies as a function of altitude, was computed and included in comparison of the $Fe^+$ measurements. Other NGIMS L2 products were used for critical ancillary data sets, such as neutral atmospheric densities and total ionospheric densities. We restrict all data sets to the inbound leg only to avoid skews in the neutral $CO_2$ densities due to gas accumulation post-periapsis (see Stone et al., 2018).

A key difference between our analysis and that presented in Grebowsky et al. (2017) is the numerical approach used to calculate the average metallic ion density as a function of altitude. In Grebowsky et al. (2017), vertical profiles of metal ion densities were constructed using a geometric average at each altitude bin, that is, $\langle n(z \pm \Delta z)\rangle = \sqrt[k]{n_1 n_2 \dots n_k}$, where $n_i$ are the individual metallic ion density measurements within altitudes of $z \pm \Delta z$ and $k$ is the total number of observations in such altitude bin. The underlying motivation for using a geometric average as opposed to an arithmetic average is the large logarithmic range over which metal ion densities were observed at a given altitude. In cases where the metallic ion densities were measured to be zero, such values were replaced with $n_i = 10^{-6}$ $cm^{-3}$ in order to prevent the geometric average from returning zero. For our analysis, we elected not to replace zero values with $10^{-6}$ as we suspected that such replacement may artificially bias the geometric average to lower values. We investigated three alternate methods of averaging the data, including a simple arithmetic mean, the median, and a mixed approach where we first calculated the geometric average at each altitude for all NGIMS metallic ion measurements that were not equal to zero and then

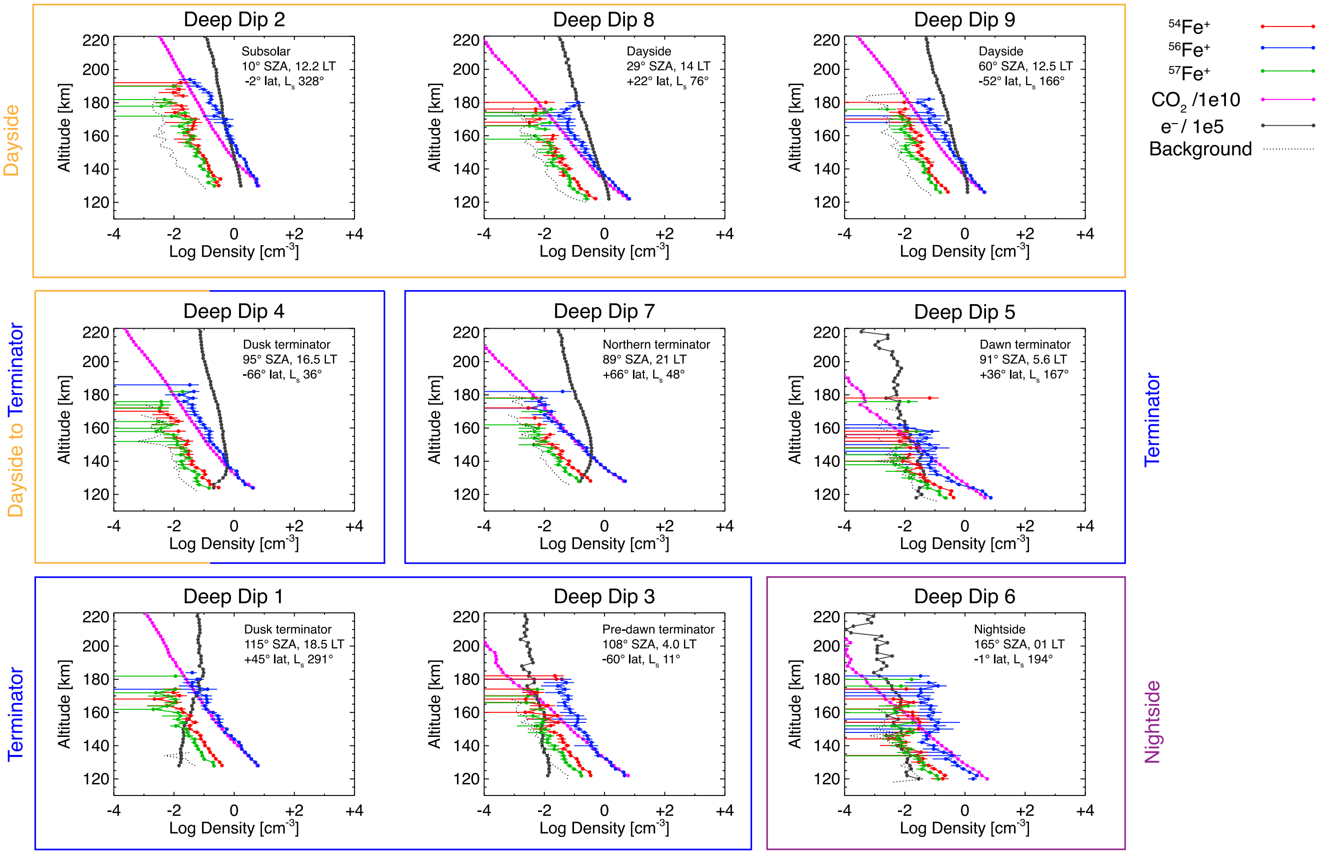


**Figure 1.** Altitude abundance profiles of the three iron isotopes, $^{54}Fe^+$, $^{56}Fe^+$, and $^{57}Fe^+$, for the inbound leg of each of the nine MAVEN Deep Dip campaigns, organized primarily by solar zenith angle. Also plotted in each panel are the neutral $CO_2$ and ionospheric electron density, scaled down by $10^{10}$ and $10^5$, respectively, for comparison, as well as the metallic ion background rate (dotted line). The statistical error to the mean is plotted for each $Fe^+$ measurements and in many cases, is smaller than the symbol size.

linearly weighted this geometric mean with the fraction of data points in the ensemble not equal to zero. We found that these three methods generally returned consistent results, with the exception of the median toward higher altitudes which often also returned zero due to lower metallic ion densities. These methods also tended to yield a different result for the metallic ion densities compared to that used in Grebowsky et al. (2017). For our analysis here, we adopted the simple arithmetic mean throughout all calculations. Further discussion of this methodology and its comparison to the Grebowsky et al. (2017) results is presented in the Supplemental Information (Figures S1–S4 in Supporting Information S1).

## 3. Results

### 3.1. Deep Dip Abundance Profiles

Figure 1 shows the $Fe^+$ abundance profiles as a function of altitude for the inbound segments of the nine MAVEN Deep Dip (DD) campaigns. The DDs consist of ∼15 consecutive orbits at diverse locations where the MAVEN periapsis is lowered to ∼125 km in order to measure connections between Mars' upper and lower atmosphere (see Jakosky et al., 2015). The DDs shown in Figure 1 are organized primarily by increasing solar zenith angle, with three occurring on the martian dayside (DDs 2, 8, 9), one that transitions from dayside to the terminator (DD 4), four occurring along the terminators (either dawn or dusk; DDs 7, 5, 1, 3), and one on the martian nightside (DD 6). Each panel also shows the neutral $CO_2$ density scaled down by $10^{10}$ and the ionospheric electron density scaled down by $10^5$ for comparison. In nearly all DDs, the primary iron isotope, $^{56}Fe^+$, attains densities of $\sim 10$ cm$^{-3}$ near 120 km with only DD 6 on the martian nightside having a lower maximum $^{56}Fe^+$ density of $\sim 2$ cm$^{-3}$. The $^{56}Fe^+$ density as observed by NGIMS is highly significant compared to background (dashed line), with signal-to-noise ratios of ∼100. The two minor iron isotopes, $^{54}Fe^+$ and $^{57}Fe^+$, have lower densities than that of the $^{56}Fe^+$

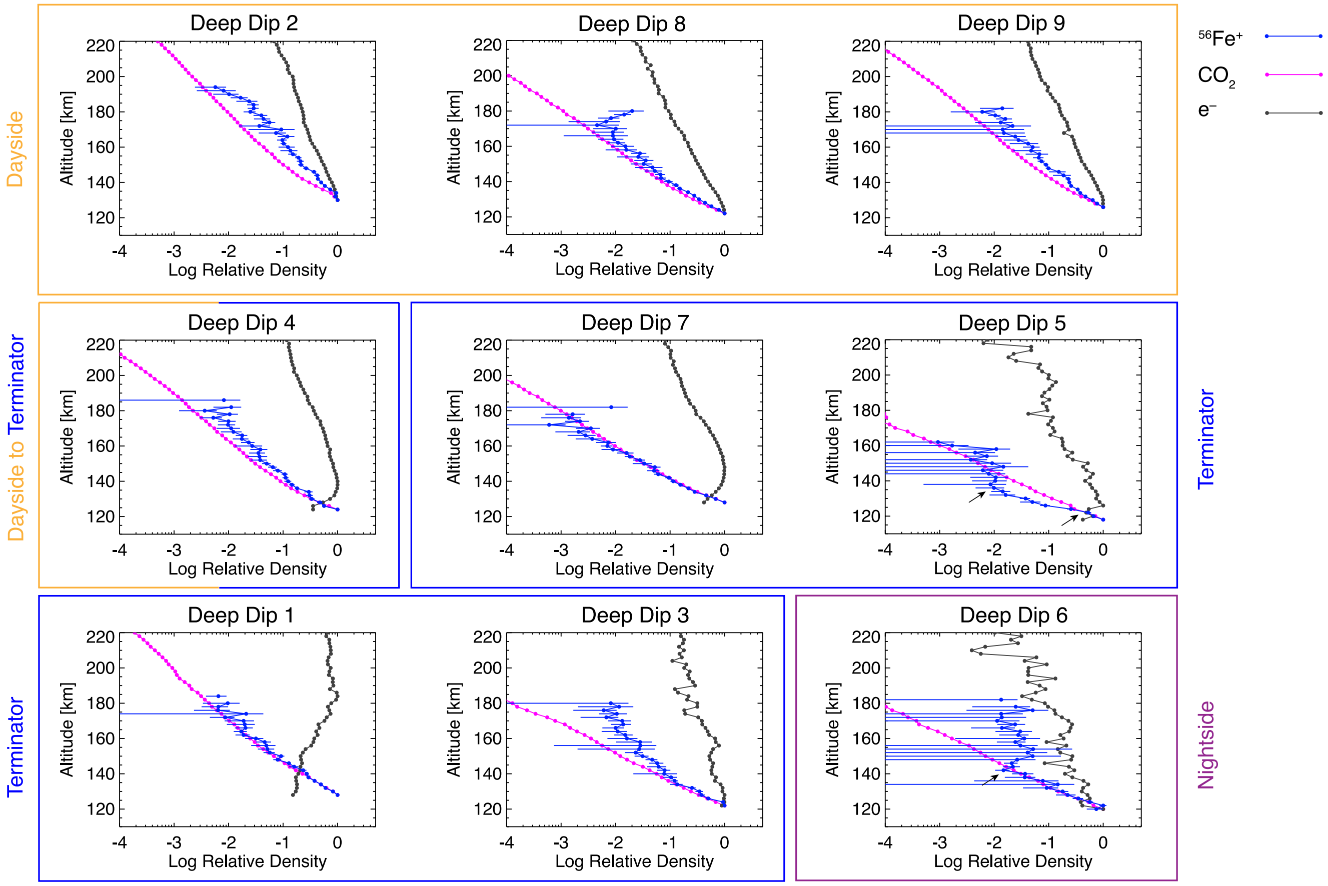


**Figure 2.** Relative altitude abundance profiles of $^{56}Fe^+$, neutral $CO_2$, and ionospheric electron density for the inbound leg of each of the nine MAVEN Deep Dip campaigns, organized primarily by solar zenith angle. All curves have been normalized to their maximum value, regardless of the altitude at which it occurs. Arrows in the DD5 and DD6 panels corresponds to points discussed in the main text.

isotope, with typical peak densities at the lowest altitudes between $\sim 0.1-1$ cm$^{-3}$, with DD 6 again having the lowest maximum abundances. The $^{54}Fe^+$ and $^{57}Fe^+$ isotopes naturally have lower signal-to-noise ratios than $^{56}Fe^+$ and in some cases (e.g., DD 5 and 6) do not have statistically significant detections at some altitudes.

The vertical structure of the $Fe^+$ abundance is more clearly analyzed by inspecting the normalized altitude profiles, shown in Figure 2, where we have displayed only $^{56}Fe^+$ for clarity. Here, all abundances have been normalized to their maximum observed value, regardless of altitude, and variations in the behavior of the vertical $Fe^+$ structure can be seen across different DDs. In DD 2 which occurred near the subsolar point, the $Fe^+$ ions maintain scale heights larger than the neutral $CO_2$ yet smaller than the bulk ionospheric plasma. DDs 8, 9, 4, and 3, which are on the dayside (8, 9), dayside-to-terminator, and terminator regions, respectively, have $Fe^+$ altitude profiles that match closely to the neutral $CO_2$ scale heights at lower altitudes (typically $<\sim$135 km) followed by gradually increasing scale heights at larger altitudes. In DDs 7 and 1, both of which occurred at the terminators, the $Fe^+$ structure closely matches the neutral $CO_2$ scale height up to altitudes of 180 km. Finally, DDs 5 and 6 in the nightside-to-terminator and nightside regions, respectively, show disjoint structures as a function of altitude. DD 6 maintains a $CO_2$-like scale height up to $\sim$145 km before abruptly transitioning to a scale height identical to that of the ionosphere. DD 5 has three apparent regions, with a $CO_2$-like scale height up to 125 km, a smaller scale height smaller than the neutral $CO_2$ from 125 to 135 km, followed by an abrupt transition to an ionospheric-like scale height at altitudes greater than 135 km (see annotated arrows in Figure 2). Thus, the $Fe^+$ altitude profiles have variable conditions from one DD to another, suggesting a complex interplay of various effects, discussed further in Section 4.

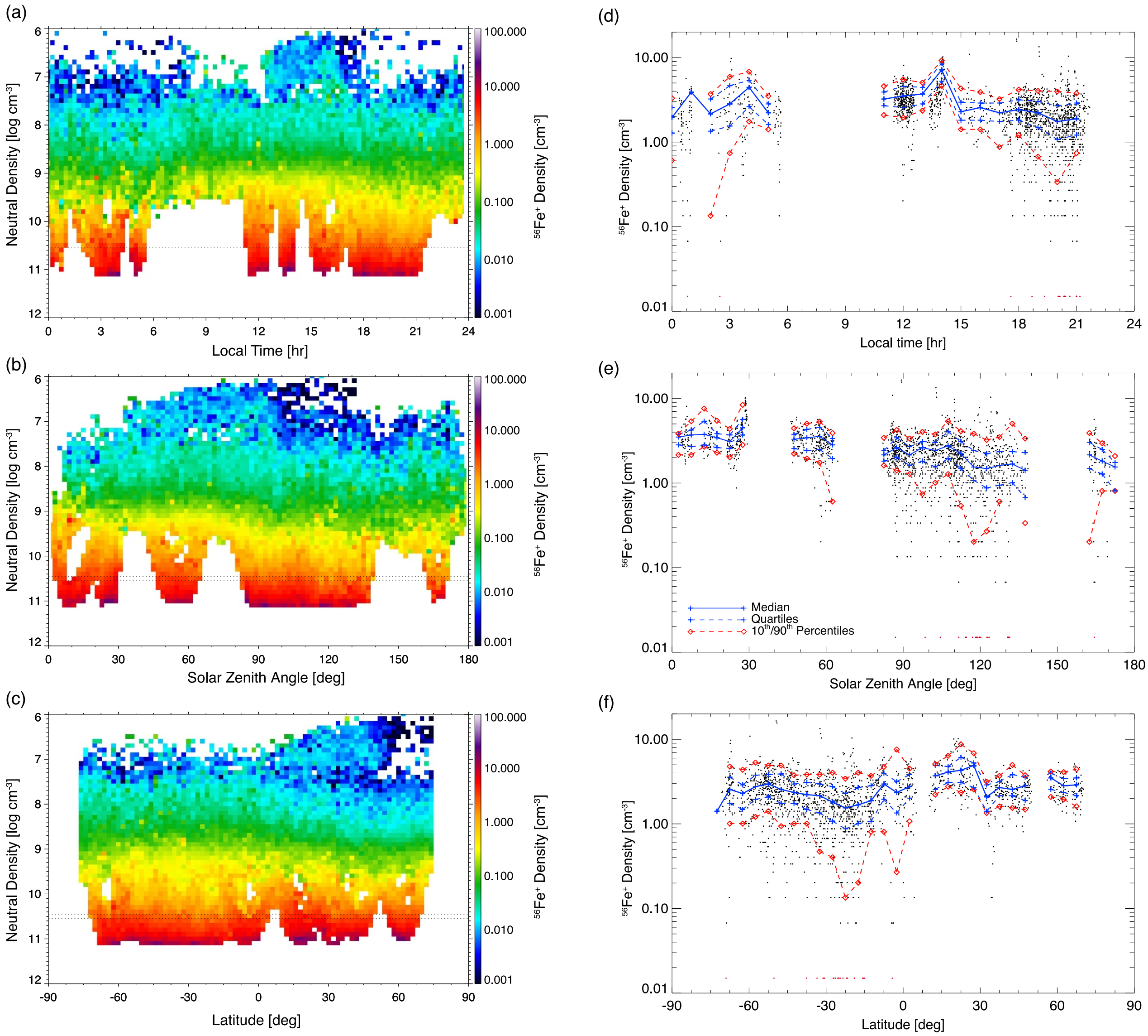


**Figure 3.** (a–c) The local time, solar zenith angle, and latitude density distributions, respectively, versus neutral density for $^{56}Fe^{+}$ averaged over January 2015 to October 2020 over the approximately altitude range of 120−180 km. Dashed lines represent the slice of observations shown in panels (d–f). (d–f) The distributions of individual NGIMS $Fe^{+}$ density measurements as a function of local time, solar zenith angle, and latitude, respectively, within neutral densities of $\log n = [10.45, 10.55]$ $cm^{-3}$. Also denoted as the medians, quartiles and 10%/90% levels. Individual measurements that reported zero density are marked as red dots at a value of 0.015 $cm^{-3}$.

### 3.2. Global Meteoric $Fe^{+}$ Distribution

Figures 3a–3c shows the global distributions of $^{56}Fe^{+}$ ions averaged over the time period of January 2015 to October 2020 as a function of (a) local time versus neutral density, (b) solar zenith angle versus neutral density, and (c) latitude versus neutral density. Nominal (i.e., non-Deep Dip) MAVEN periapses occur near $\log(n\ [cm^{-3}]) \sim 9.5$ while the Deep Dips can be seen as distinct excursions down to lower neutral densities near $\log(n\ [cm^{-3}]) \sim 11$. To first order, the primary variation in $^{56}Fe^{+}$ densities is as a function of neutral density (altitude), with only second-order variation seen in local time, solar zenith angle, or latitude. Within the range measured by MAVEN/NGIMS, the average $^{56}Fe^{+}$ density ranges from ∼50 $cm^{-3}$ at the lowest altitudes to $10^{-3}$ $cm^{-3}$ at the highest altitudes. Slight variations are present in each of the distributions. At neutral densities at or greater than $\log(n\ [cm^{-3}]) \sim 9.0$, densities rise slightly on the martian dayside, seen in both local times 6–18, panel 3(a), and solar zenith angles <90°, panel 3(b). Densities are also slightly higher in the southern hemisphere than in the northern hemisphere, seen in panel 3(c).

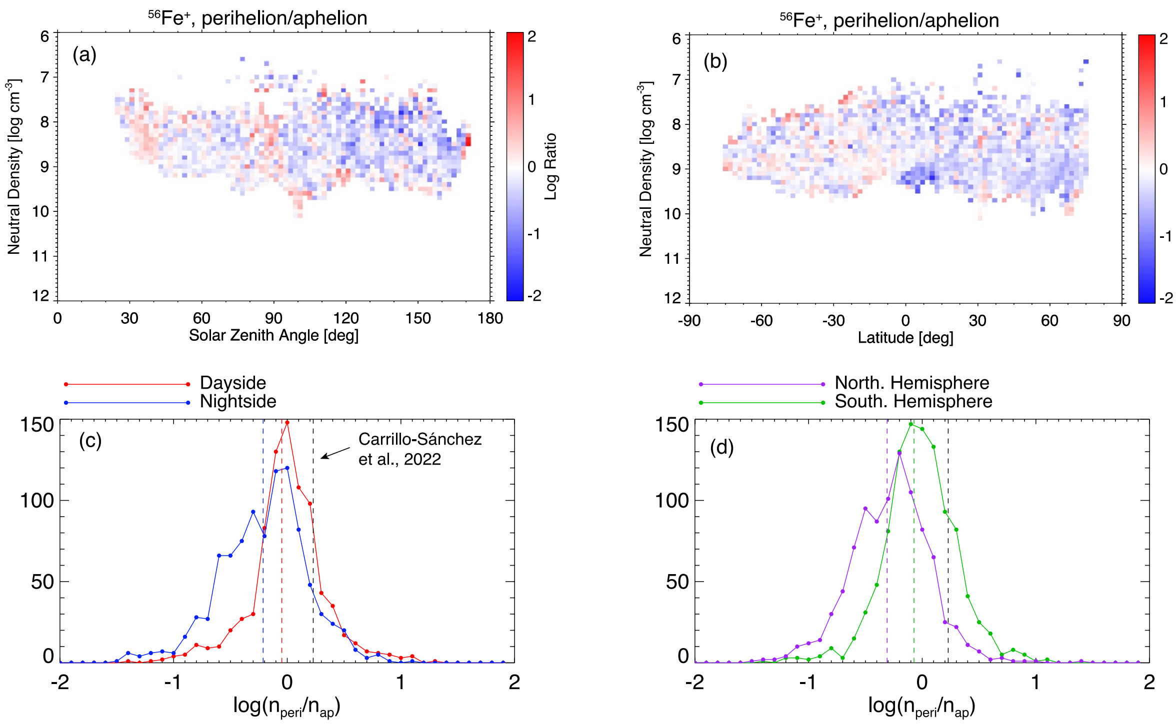


**Figure 4.** The ratio of $^{56}Fe^{+}$ densities between perihelion and aphelion as a function of panel (a) solar zenith angle and neutral density and (b) latitude and neutral density. The distribution of perihelion-to-aphelion ratios for panel (c) dayside and nightside and (d) northern hemisphere and southern hemisphere, respectively. The black dashed line is the ratio of the perihelion-to-aphelion interplanetary dust mass influx predicted by Carrillo-Sánchez et al. (2022).

To better demonstrate the $^{56}Fe^{+}$ variability, Figures 3d–3f show scatterplots of the individual $^{56}Fe^{+}$ density measurements as a function of each parameter (local time, solar zenith angle, latitude) within neutral density levels of $\log(n\ [\mathrm{cm}^{-3}]) = [10.45, 10.55]$, denoted by the dashed horizontal lines in panels 3(a–c). Also shown are the median, quartiles (25%, 75%), and 10%/90% levels of the $^{56}Fe^{+}$ density. As seen in both the local time and solar zenith angle distributions, the $^{56}Fe^{+}$ density near the sub-solar point (LT ∼12–15 hr; SZA <50°) is tightly contained between ∼2–8 $\mathrm{cm}^{-3}$ at the 10%/90% level, with median values only ranging from ∼3 to 5 $\mathrm{cm}^{-3}$. Progressing toward the terminator and onto the nightside (LT <6 or LT >18; SZA >60°), the median value drops by a factor of approximately two to densities of ∼1–2 $\mathrm{cm}^{-3}$. Notably, however, the quartiles and 10%/90% levels expand signifying a greater spread in the individual observations. A significant number of low-density (∼0.1−1 $\mathrm{cm}^{-3}$) observations are present in the martian nightside, pulling the 10% level down to values as low as 0.2 $\mathrm{cm}^{-3}$. Simultaneously, there exists approximately a half-dozen individual observations at densities >10 $\mathrm{cm}^{-3}$, higher than that observed on the dayside, likely due to the presence of sporadic-E layers (e.g., Collinson et al., 2020; Grebowsky et al., 2017).

We have also examined the variability of the $^{56}Fe^{+}$ ion abundance over a martian orbit to test for any changes that may be present due to, e.g., variation in the overall interplanetary dust flux to Mars (e.g., Carrillo-Sánchez et al., 2022) or due to possible changes in atmospheric photochemistry or circulation as suggested based on MAVEN observations of $Mg^{+}$ variability (e.g., Crismani et al., 2023). Figure 4 compares the $Fe^{+}$ distributions as a function of solar zenith angle and neutral density (left column) and as a function of latitude and neutral density (right column), between 90° $L_s$ portions of the orbit centered at perihelion and aphelion. Due to limitations in the data coverage, the primary region of overlap in observations between perihelion and aphelion occurs between neutral densities of $\log(n\ [\mathrm{cm}^{-3}]) = [10, 7]$. As seen in both the spatial distributions, panels 4(a) and (b), as well as in the histogram of all ratios shown in panels 4(c) and (d), the ratio of perihelion-to-aphelion $^{56}Fe^{+}$ densities are skewed to less than unity, that is, there tends to be less $^{56}Fe^{+}$ at perihelion. Furthermore, $^{56}Fe^{+}$ densities at perihelion tend to be even lower on the nightside (blue curve, panel 4(c)) and in the northern hemisphere (purple curve, 4(d)). In comparison, the predicted ratio of perihelion-to-aphelion total ablated Fe mass flux by Carrillo-Sánchez et al. (2022), $\log_{10}(0.22\ \mathrm{tons\ sol}^{-1}/0.13\ \mathrm{tons\ sol}^{-1}) = +0.23$, shown as the dashed line, is notably greater than the observed median. Thus, despite a likely increase in the total amount of ablated meteoritic Fe injected into Mars' atmosphere, the net $Fe^+$ density is reduced at perihelion.

## 4. Discussion

First, we compare our findings here with the earlier report on metallic ion distributions published in Grebowsky et al. (2017). Due to the differences in data reduction and averaging used here, we arrive at different solutions for the specific profiles of the individual Deep Dips analyzed in Grebowsky et al. (2017), namely DDs 1−4 (cf., their Figure 3 and Figures S1–S4 in Supporting Information S1). DD 2 remains the closest comparison between Grebowsky et al. (2017) and our results here with a clear departure of the $^{56}Fe^+$ profiles to higher scale heights than the neutral $CO_2$ at an altitude of ∼135 km. DDs 3 and 4 shown in Grebowsky et al. (2017) have marked declines in the $Fe^+$ profiles with scale heights below the neutral $CO_2$ that are not seen in our analysis. Instead, we find that DDs 3 and 4 have profiles that are similar to DD 2, matching the neutral scale height at lower altitudes before transitioning to a larger scale height at altitudes near ∼130 km. Finally, in Grebowsky et al. (2017), DD 1 shows a split behavior with an $Fe^+$ scale height slightly larger than the neutral $CO_2$ before abruptly transitioning to a much colder scale height near 150 km. In contrast, our results for DD 1 show that the $Fe^+$ profile matches the neutral $CO_2$ scale height up to altitudes of at least 180 km. Overall, the differences between our derived $Fe^+$ profiles and those presented in Grebowsky et al. (2017) can be understood as a function of the averaging method, whereby the replacement of zeroes by values of $10^{-6}$ $cm^{-3}$ in the geometric average inadvertently pulled the $Fe^+$ density too low.

The diversity of $Fe^+$ profiles seen in the nine MAVEN Deep Dips is a likely reflection of the complex and variable mixture of processes acting on these minor ions, primarily molecular diffusion, ambipolar electric fields, gyromotion around magnetic fields, and ion-neutral collisions. First, recall that meteoric ions are deposited in the martian atmosphere at altitudes between 70 and 100 km (e.g., Crismani et al., 2023; Plane, Carrillo-Sánchez, et al., 2018), much lower than NGIMS samples. Thus, the ion densities observed by NGIMS at altitudes >120 km are nearly entirely a result of upwards ion transport processes. Within their primary deposition layer of 70−100 km, the $Fe^+$ ions undergo photochemical reactions (e.g., Whalley & Plane, 2010) and upwards transport by a combination of eddy and molecular diffusion, the balance of which is controlled by the homopause altitude (typically between 60−120 km; e.g., Slipski et al., 2018; Yoshida et al., 2020). As the $Fe^+$ ions reach the lowest altitudes that MAVEN/NGIMS can sample near ∼120 km, photochemical processes likely become negligible with estimated $Fe^+$ lifetimes between 40−1,000 hr (Whalley & Plane, 2010). While molecular diffusion of $Fe^+$ ions alone would yield vertical density profiles with scale heights less than the neutral $CO_2$ (assuming equal temperatures), the $Fe^+$ ions are also influenced by the relative strengths of ion-neutral collisions and electromagnetic fields. In the lowest altitude range, the ion-neutral collision frequency is much greater than the ion cyclotron frequency (i.e., $\nu_{in} \gg \Omega_{Fe+}$) and thus, the $Fe^+$ bulk ion motion should be fully coupled to the presence of any neutral winds, thereby preventing the ions from undergoing any electromagnetic drifts. As altitudes increase, there exists an intermediate region where the ion-neutral collision frequency is on the order of the cyclotron frequency (i.e., $\nu_{in} \sim \Omega_{Fe+}$) and here, the $Fe^+$ ions will tend to drift along the direction of any background electric fields (i.e., related to the formation of Pedersen currents). Finally, at the highest altitude range, the ion cyclotron frequency surpasses the ion-neutral collision frequency ($\Omega_{Fe+} > \nu_{in}$) and the ions undergo the full suite of relevant electromagnetic drifts (e.g., ambipolar, ExB, gradient-curvature, etc.). Within this conceptual framework, there exists significant variability in the ion-neutral collision frequencies, magnetic field strength and orientation, and ion temperature, all of which contribute to $Fe^+$ altitude profile. For example, Lillis et al. (2019) have shown that under typical dayside conditions in non-crustal magnetic field regions, the ion-magnetization altitude for $O_2^+$ ions (mass 32 amu) is ∼180 km. Under these conditions, $Fe^+$ ions (mass 56 amu) would have lower gyrofrequencies and higher magnetization altitudes, implying that most $Fe^+$ observations would be within the highly neutral-collision-dominated region and thus, more likely to follow neutral scale heights. In contrast, any $Fe^+$ measurements that fall within regions of increased magnetic field strength would have higher gyrofrequencies, lower ion-magnetization altitudes, and a greater influence of drifts along the electric field direction. A full explanation of the $Fe^+$ altitude profiles seen in each DD likely requires a detailed examination of the relative gyro- and ion-neutral collision frequencies on each orbit, as the underlying rotation of Mars between each ∼4.5-hr MAVEN orbit changes the crustal field underfoot by factors of 10 or greater (e.g., Langlais et al., 2019; D. L. Mitchell et al., 2007).

Finally, the $Fe^+$ distributions reported here at altitudes greater than 120 km provide a critical comparison point for MAVEN/IUVS observations of $Mg^+$ ions, which range from 60−160 km (Crismani et al., 2017, 2023). These observations have shown that the $Mg^+$ distributions have an overall dawn-to-dusk variability on the order of a factor of two and significant latitudinal variability within each given martian season. The $Mg^+$ density at 90 km drops by a factor of two from dawn to dusk, yet at 120 km, increases by at least a factor of two between dawn and mid-afternoon (∼15 LT). Additionally, the $Mg^+$ distributions show a peak in the northern hemisphere in late southern spring (slightly post-perihelion) followed by a deep depletion in the northern hemisphere near perihelion. NGIMS observations of $Fe^+$ distributions show a similar trend, with a factor of ∼50% reduction in the median $Fe^+$ in the northern hemisphere from aphelion to perihelion (i.e., Figure 4d). While the magnitude of the $Fe^+$ reduction is less than the near complete dropout seen in $Mg^+$ (Crismani et al., 2023), this correlation does suggest that both species are responding to a common set of physical processes that deplete metallic ions in the northern martian winter/perihelion. This process may be related to changes in atmospheric photochemical pathways as a result of increased atmospheric $H_2O$ abundance due to warmer planetary temperatures at perihelion; however, more detailed photochemical modeling is required to verify this hypothesis.

## 5. Conclusion

Metallic $Fe^+$ ions are a globally distributed species in the martian ionosphere at altitudes between ∼120−180 km across all local times, solar zenith angles, latitudes, and seasons. With densities ranging from $10^{-3}$ $cm^{-3}$ to ∼50 $cm^{-3}$ between approximately 120 and 180 km, metallic $Fe^+$ densities are far less than the primary photochemical species, e.g., $O_2^+$, $CO_2^+$, $HNO^+$, $O^+$, $NO^+$, etc., that have densities of ∼$10^2$ to ∼$10^4$ $cm^{-3}$ (e.g., Lee et al., 2024). $Fe^+$ ions typically have total relative abundances of ∼$10^{-5}$ on the dayside and ∼$10^{-3}$ on the nightside. $Fe^+$ densities are variable as a function of solar zenith angle, latitude, and season; however, the overall magnitude of this variability appears to be less than that seen at lower altitudes in the remotely sensed $Mg^+$ distributions (Crismani et al., 2017, 2023). Nevertheless, it is likely that both species are responding to common transport and/or chemical processes in the martian ionosphere (e.g., Whalley & Plane, 2010). Thus, further research into both the photochemical evolution and transport processes of $Fe^+$ ions is the martian ionosphere is warranted to better understand both the bulk variations seen in the $Fe^+$ densities and the individual DD profiles. Finally, these observations also provide an important comparative data set for understanding metallic ion behavior at Earth, including in situ and/or remote sensing measurements and associated modeling (e.g., Chu et al., 2020; Wu et al., 2021; Yu et al., 2022).

## Data Availability Statement

All MAVEN mission data used in this study are publicly available on the NASA Planetary Data System, including SWEA (D. Mitchell, 2017), MAG (Connerney, 2017), and NGIMS (Elrod, 2014). Derived NGIMS results presented in this study can be accessed at Poppe (2025).

**Acknowledgments**

A.R.P. and G.A.C. acknowledge NASA's Mars Data Analysis Program, Grant 80NSSC24K0924. A.R.P. thanks D. Mitchell and R. J. Lillis for support in accessing and interpreting MAVEN data, and K. G. Hanley for discussions on ion temperatures in the Martian ionosphere. J.M.C.P. acknowledges funding from the UK STFC, Grant ST/T000279/1.

## References

Aikin, A. C., & Goldberg, R. A. (1973). Metallic ions in the equatorial ionosphere. *Journal of Geophysical Research*, *78*(4), 734–745. https://doi.org/10.1029/ja078i004p00734

Benna, M., Bougher, S. W., Lee, Y., Roeten, K. J., Yigit, E., Mahaffy, P. R., & Jakosky, B. M. (2019). Global circulation of Mars' upper atmosphere. *Science*, *366*(6471), 1363–1366. https://doi.org/10.1126/science.aax1553

Benna, M., Mahaffy, P. R., Grebowsky, J. M., Plane, J. M. C., Yelle, R. V., & Jakosky, B. M. (2015). Metallic ions in the upper atmosphere of Mars from the passage of comet C/2013 A1 (Siding Spring). *Geophysical Research Letters*, *42*(12), 4670–4675. https://doi.org/10.1002/2015GL064159

Carrillo-Sánchez, J. D., Gómez-Martín, J. C., Bones, D. L., Nesvorný, D., Pokorný, P., Benna, M., et al. (2020). Cosmic dust fluxes in the atmospheres of Earth, Mars, and Venus. *Icarus*, *335*, 113395. https://doi.org/10.1016/j.icarus.2019.113395

Carrillo-Sánchez, J. D., Janches, D., Plane, J. M. C., Pokorný, P., Sarantos, M., Crismani, M. M. J., et al. (2022). A modeling study of the seasonal, latitudinal, and temporal distribution of the meteoroid mass input at mars: Constraining the deposition of meteoric ablated metals in the upper atmosphere. *Plant Science (Limerick, Ireland) J.*, *3*(239), 239. https://doi.org/10.3847/PSJ/ac8540

Carrillo-Sánchez, J. D., Nesvorný, D., Pokorný, P., Janches, D., & Plane, J. M. C. (2016). Sources of cosmic dust in the Earth's atmosphere. *Geophysical Research Letters*, *43*(23), 11979–11986. https://doi.org/10.1002/2016gl071697

Chu, X., Nishimura, Y., Xu, Z., Yu, Z., Plane, J. M. C., Gardner, C. S., & Ogawa, Y. (2020). First simultaneous lidar observations of thermosphere-ionosphere Fe and Na (TIFe and TINa) layers at McMurdo (77.84°S, 166.67°E), Antarctica with concurrent measurements of auroral activity, enhanced ionization layers, and converging electric field. *Geophysical Research Letters*, *47*(20). https://doi.org/10.1029/2020GL090181

Collinson, G. A., McFadden, J., Grebowsky, J., Mitchell, D., Lillis, R., Withers, P., et al. (2020). Constantly forming sporadic E-like layers and rifts in the Martian ionosphere and their implications for Earth. *Nature Astronomy*, *4*(5), 486–491. https://doi.org/10.1038/s41550-019-0984-8

Connerney, J. (2017). *MAVEN magnetometer (MAG) calibrated data bundle*. NASA Planetary Data System. https://doi.org/10.17189/1414178

Crismani, M. M. J., Deighan, J., Schneider, N. M., Plane, J. M. C., Withers, P., Halekas, J., et al. (2019). Localized ionization hypothesis for transient ionospheric layers. *Journal of Geophysical Research: Space Physics*, *124*(6), 4870–4880. https://doi.org/10.1029/2018JA026251

Crismani, M. M. J., Schneider, N. M., Plane, J. M. C., Evans, J. S., Jain, S. K., Chaffin, M. S., et al. (2017). Detection of a persistent meteoric metal layer in the Martian atmosphere. *Nature Geoscience*, *10*(6), 401–404. https://doi.org/10.1038/NGEO2958

Crismani, M. M. J., Tyo, R., Schneider, N., Plane, J., Feng, W., Carrillo-Sánchez, J.-D., et al. (2023). Martian meteoric Mg+: Atmospheric distribution and variability from MAVEN/IUVS. *Journal of Geophysical Research: Planets*, *128*(1). https://doi.org/10.1029/2022je007315

Elrod, M. (2014). *MAVEN neutral gas and ion mass spectrometer data*. NASA Planetary Data System. https://doi.org/10.17189/1518931

Grebowsky, J. M., & Aikin, A. C. (2002). In situ measurements of meteoric ions. In E. Murad & I. P. Williams (Eds.), *Meteors in the earth's atmosphere (chap. 8)*. Cambridge University Press.

Grebowsky, J. M., Benna, M., Plane, J., Collinson, G., Mahaffy, P., & Jakosky, B. (2017). Unique, non-earthlike, meteoritic ion behavior in upper atmosphere of mars. *Geophysical Research Letters*, *44*(7), 3066–3072. https://doi.org/10.1002/2017gl072635

Gumbel, J., & Megner, L. (2009). Charged meteoric smoke as ice nuclei in the mesosphere: Part 1–A review of basic concepts. *Journal of Atmospheric and Solar-Terrestrial Physics*, *71*(12), 1225–1235. https://doi.org/10.1016/j.jastp.2009.04.012

Haider, S. A., Pandya, B. M., & Molina-Cuberos, G. J. (2013). Nighttime ionosphere caused by meteoroid ablation and solar wind electron-proton-hydrogen impact on Mars: MEX observation and modeling. *Journal of Geophysical Research: Space Physics*, *118*, 6786–6794. https://doi.org/10.1002/jgra.50590

Hartwick, V. L., Toon, O. B., & Heavens, N. G. (2019). High-altitude water ice cloud formation on Mars controlled by interplanetary dust particles. *Nature Geoscience*, *12*(7), 516–521. https://doi.org/10.1038/s41561-019-0379-6

Jakosky, B. M., Lin, R. P., Grebowsky, J. M., Luhmann, J. G., Mitchell, D. F., Beutelschies, G., et al. (2015). The Mars atmosphere and volatile evolution (MAVEN) mission. *Space Science Reviews*, *195*(1–4), 3–48. https://doi.org/10.1007/s11214-015-0139-x

Langlais, B., Thébault, E., Houliez, A., Purucker, M. E., & Lillis, R. J. (2019). A new model of the crustal magnetic field of Mars using MGS and MAVEN. *Journal of Geophysical Research: Planets*, *124*, 1542–1569. https://doi.org/10.1029/2018JE005854

Lee, Y., Benna, M., & Mahaffy, P. (2024). The dayside ionosphere of Mars observed by MAVEN NGIMS. *Icarus*, *420*, 116192. https://doi.org/10.1016/j.icarus.2024.116192

Lillis, R. J., Fillingim, M. O., Ma, Y., Gonzalez-Galindo, F., Forget, F., Johnson, C. L., et al. (2019). Modeling wind-driven ionospheric dynamo currents at Mars: Expectations for InSight magnetic field measurements. *Geophysical Research Letters*, *46*(10), 5083–5091. https://doi.org/10.1029/2019GL082536

Listowski, C., Määttänen, A., Montmessin, F., Spiga, A., & Lefèvre, F. (2014). Modeling the microphysics of CO2 ice clouds within wave-induced cold pockets in the martian mesosphere. *Icarus*, *237*, 239–261. https://doi.org/10.1016/j.icarus.2014.04.022

Mahaffy, P. R., Benna, M., King, T., Harpold, D. N., Arvey, R., Barciniak, M., et al. (2015). The neutral gas and ion mass spectrometer on the Mars atmosphere and volatile evolution mission. *Space Science Reviews*, *195*(1–4), 49–73. https://doi.org/10.1007/s11214-014-0091-1

Megner, L., & Gumbel, J. (2009). Charged meteoric particles as ice nuclei in the mesosphere: Part 2–A feasibility study. *Journal of Atmospheric and Solar-Terrestrial Physics*, *71*(12), 1236–1244. https://doi.org/10.1016/j.jastp.2009.05.002

Mitchell, D. (2017). *MAVEN solar wind electron analyzer (SWEA) calibrated data bundle*. NASA Planetary Data System. https://doi.org/10.17189/1414181

Mitchell, D. L., Lillis, R. J., Lin, R. P., Connerney, J. E. P., & Acuña, M. H. (2007). A global map of Mars' crustal magnetic field based on electron reflectometry. *Journal of Geophysical Research*, *112*(E1), E01002. https://doi.org/10.1029/2005JE002564

Moses, J. I. (1992). Meteoroid ablation in Neptune's atmosphere. *Icarus*, *99*(2), 368–383. https://doi.org/10.1016/0019-1035(92)90153-x

Moses, J. I., & Poppe, A. R. (2017). Dust ablation on the giant planets: Consequences for stratospheric photochemistry. *Icarus*, *297*, 33–58. https://doi.org/10.1016/j.icarus.2017.06.002

Pätzold, M., Tellmann, S., Häusler, B., Hinson, D., Schaa, R., & Tyler, G. L. (2005). A sporadic third layer in the ionosphere of Mars. *Science*, *310*(837), 837–839. https://doi.org/10.1126/science.1117755

Pesnell, W. D., & Grebowsky, J. (2000). Meteoric magnesium ions in the Martian atmosphere. *Journal of Geophysical Research*, *105*(E1), 1695–1707. https://doi.org/10.1029/1999je001115

Plane, J. M. C., Carrillo-Sánchez, J. D., Mangan, T. P., Crismani, M. M. J., Schneider, N. M., & Määttänen, A. (2018). Meteoric metal chemistry in the martian atmosphere. *Journal of Geophysical Research: Planets*, *123*, 695–707. https://doi.org/10.1002/2017JE005510

Plane, J. M. C., Flynn, G. J., Määttänen, A., Moores, J. E., Poppe, A. R., Carrillo-Sánchez, J. D., & Listowski, C. (2018). Impacts of cosmic dust on planetary atmospheres and surfaces. *Space Science Reviews*, *214*(23), 23. https://doi.org/10.1007/s11214-017-0458-1

Poppe, A. R. (2025). Dataset for "MAVEN observations of metallic Fe+ distributions in the martian ionosphere". https://doi.org/10.5281/zenodo.15097646

Slipski, M., Jakosky, B. M., Benna, M., Elrod, M., Mahaffy, P., Kass, D., et al. (2018). Variability of the martian turbopause altitudes. *Journal of Geophysical Research: Planets*, *123*(11), 2939–2957. https://doi.org/10.1029/2018JE005704

Stone, S. W., Yelle, R. V., Benna, M., Elrod, M. K., & Mahaffy, P. R. (2018). Thermal structure of the martian upper atmosphere from MAVEN NGIMS. *Journal of Geophysical Research: Planets*, *123*(11), 2842–2867. https://doi.org/10.1029/2018JE005559

Whalley, C. L., & Plane, J. M. C. (2010). Meteoric ion layers in the Martian atmosphere. *Faraday Discussions*, *147*, 349–369. https://doi.org/10.1039/c003726e

Withers, P., Christou, A. A., & Vaubaillon, J. (2013). Meteoric ions layers in the ionospheres of Venus and Mars: Early observations and consideration of the role of meteor showers. *Advances in Space Research*, *52*(7), 1207–1216. https://doi.org/10.1016/j.asr.2013.06.012

Withers, P., Mendillo, M., Hinson, D. P., & Cahoy, K. (2008). Physical characteristics and occurrence rates of meteoric plasma layers detected in the Martian ionosphere by the Mars Global Surveyor Radio Science Experiment. *Journal of Geophysical Research*, *113*(A12), A12314. https://doi.org/10.1029/2008ja013636

Wu, J., Feng, W., Liu, H.-L., Xue, X., Marsh, D. R., & Plane, J. M. C. (2021). Self-consistent global transport of metallic ions with WACCM-X. *Atmospheric Chemistry and Physics*, *21*(20), 15619–15630. https://doi.org/10.5194/acp-21-15619-2021

Yoshida, N., Nakagawa, H., Terada, N., Evans, J. S., Schneider, N. M., Jain, S. K., et al. (2020). Seasonal and latitudinal variations of dayside N2/CO2 ratio in the martian thermosphere derived from MAVEN IUVS observations. *Journal of Geophysical Research: Planets*, *125*(12). https://doi.org/10.1029/2020JE006378

Yu, B., Xue, X., Scott, C. J., Jia, M., Feng, W., Plane, J. M. C., et al. (2022). Comparison of middle- and low-latitude sodium layer from a ground-based lidar network, the Odin satellite, and WACCM-Na model. *Atmospheric Chemistry and Physics*, *22*(17), 11485–11504. https://doi.org/10.5194/acp-22-11485-2022